COMMUNICATION

Enhanced Li-Ion Conductivity in $LiBH_4$-ZrO_2 Nanocomposites and Nanoscale Li Imaging by Energy-Filtered Transmission Electron Microscopy

Received 00th January 20xx,
Accepted 00th January 20xx

DOI: 10.1039/x0xx00000x

Yuki Nakagawa,*[a] Tsubasa Sendo[b] and Tamaki Shibayama[a]

A complementary solid-state nuclear magnetic resonance and transmission electron microscopy (TEM) analysis was performed for $LiBH_4$-ZrO_2 nanocomposites. As a result, amorphous $LiBH_4$ films with thicknesses of less than 30 nm were observed covering the ZrO_2 particles. Li imaging by energy-filtered TEM is useful for the real-space characterization of nanoscale $LiBH_4$.

Lithium-ion batteries are widely used in a variety of energy storage applications ranging from small portable electronics to electric vehicles. However, organic liquid electrolytes typically have reduced battery lifetimes and involve the risk of electrolyte leakage.[1-3] Solid-state electrolytes are promising alternatives because they have a relatively high Li^+ transference number, high stability over a wide temperature range, and high energy density.[1-3] Among the various types, complex hydride Li-ion conductors, such as $LiBH_4$,[4,5] $Li_2B_{12}H_{12}$,[6,7] and $LiAlH_4$,[8,9] represent a new class of solid electrolytes. Lithium borohydride ($LiBH_4$) is one of the well-studied complex hydride Li-ion conductors. $LiBH_4$ has an orthorhombic low-temperature phase at room temperature (RT) that exhibits poor ion conductivity, but it undergoes a phase transition to form a hexagonal high-temperature phase at approximately 110 °C, and at 120 °C, superionic conductivity (~10^{-3} S·cm^{-1}) can be achieved.[4]

To improve the lithium-ion conductivity of $LiBH_4$ at RT, $LiBH_4$-oxide nanocomposites have been synthesized and studied. The ion conductivity of $LiBH_4$-SiO_2 and $LiBH_4$-Al_2O_3 composites reached as high as 10^{-4} S·cm^{-1} at RT, and it was proposed that the conductivity can be enhanced further by interface engineering.[10,11] The effects of adding various nanosized oxides have also been considered, and $LiBH_4$-ZrO_2 and $LiBH_4$-MgO composites exhibited conductivity on the order of 10^{-4} S·cm^{-1} at 30 °C.[12,13] Furthermore, Li-ion diffusion in nanoconfined $LiBH_4$-LiI-Al_2O_3 and $LiBH_4$/Al_2O_3 was investigated by solid-state nuclear magnetic resonance (NMR).[14,15] The variable-temperature ^{7}Li NMR spectra revealed the contribution from both the bulk and interface regions, and the latter regions were highly mobile, probably because of the structural disorder and space charge regions. In addition, experimental and theoretical screening of SiO_2, Al_2O_3, and ZrO_2 nanoscale oxides with $LiBH_4$ indicated that $LiBH_4$ dehydrogenation was promoted through a destabilization reaction with SiO_2 and Al_2O_3, but no destabilization products were observed with ZrO_2.[16]

In this study, the ion conductivity of $LiBH_4$-ZrO_2 nanocomposites was investigated. In a previous study, the estimated thickness of $LiBH_4$ from Brunauer-Emmett-Teller (BET) surface area measurements was up to tens of nanometers in $LiBH_4$-oxide nanocomposites.[12] Direct observation of nanoscale $LiBH_4$ by transmission electron microscopy (TEM) may confirm the previous measurements or provide further insights, and thus, several studies have conducted TEM analysis.[11,17] However, it was difficult to visualize Li in the composite with a high-magnification image. Lithium is a light element, which means its atomic scattering factor is low. Thus, it is difficult to obtain high contrast images by TEM. For instance, elemental mapping is often conducted by energy dispersive X-ray spectroscopy (EDS), but the occurrence probability of characteristic X-ray is low for light elements including Li. In the present study, complementary NMR and TEM analysis was performed. Li imaging in the composites was also conducted by energy-filtered TEM (EFTEM). Observing the Li distribution on the nanoscale is important because changes in the Li distribution often occur in the interfacial regions of battery materials.[18]

Fig. 1 (a) and (b) shows the X-ray diffraction (XRD) profiles of 25 vol.% ZrO_2 composites. The profiles of pristine ZrO_2 and $LiBH_4$ are shown in Fig. 1 (c-e). The profiles of 25 vol.% ZrO_2 composites contain the characteristic diffraction peaks of the

[a] *Faculty of Engineering, Hokkaido University, N-13, W-8, Sapporo 060-8628, Japan.*
[b] *Graduate School of Engineering, Hokkaido University, N-13, W-8, Sapporo 060-8628, Japan.*

Electronic Supplementary Information (ESI) available: [details of any supplementary information available should be included here]. See DOI: 10.1039/x0xx00000x

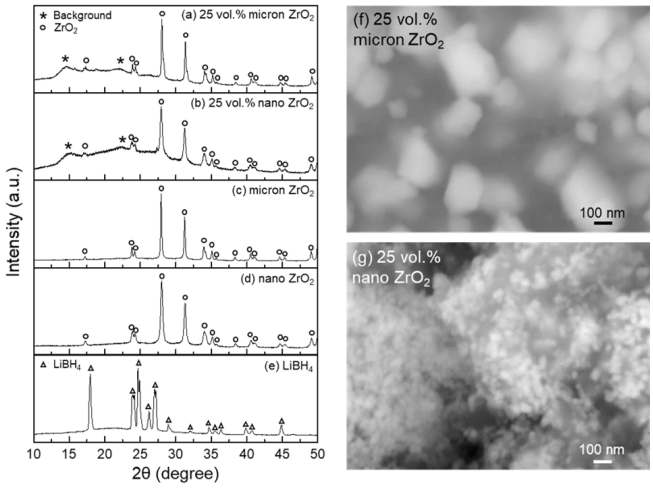

Fig. 1 XRD profiles of the (a) 25 vol.% micron ZrO_2 composite, (b) 25 vol.% nano ZrO_2 composite, (c) micron ZrO_2, (d) nano ZrO_2, and (e) $LiBH_4$. The peak intensity was normalized with respect to the maximum intensity of each profile. Cross-sectional scanning electron microscopy backscattered electron images of the (f) 25 vol.% micron ZrO_2 and (g) 25 vol.% nano ZrO_2 composite pellets.

pristine ZrO_2 phases. However, the diffraction peaks of the $LiBH_4$ phases are not observed in the composite profiles, suggesting the conversion to an amorphous state. Note that the asterisk peaks in the XRD profile are ascribed to the background from grease and the polyimide film. The $LiBH_4$ phases are also not observed for the XRD profiles of heated samples as shown in Fig. S1. Fig. 1 (f) and (g) shows the cross-sectional scanning electron microscopy backscattered electron images of the composite pellets. ZrO_2 particles with sizes in the ranges of 50–400 nm and 10–100 nm were observed in the micron ZrO_2 and nano ZrO_2 composites, respectively. Secondary electron images of the micron ZrO_2 composites are shown in Fig. S2. The ZrO_2 particles were covered with thin films, probably consisting of $LiBH_4$. Fig. 2 shows the Li-ion conductivities (σ) of the

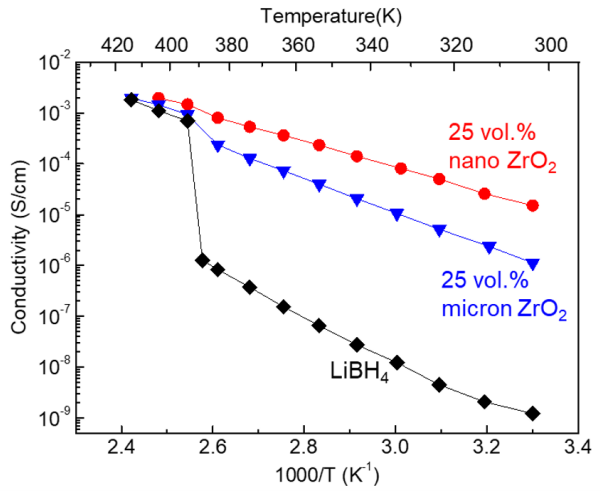

Fig. 2 Temperature-dependent Li-ion conductivity for pristine $LiBH_4$, 25 vol.% micron ZrO_2 composite, and 25 vol.% nano ZrO_2 composite.

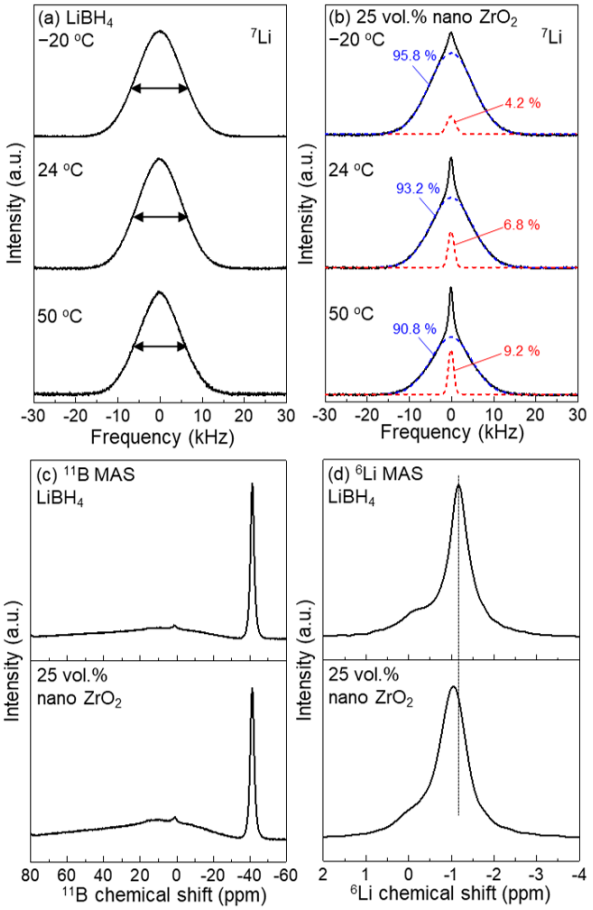

Fig. 3 Temperature-dependent ^7Li NMR spectra of (a) pristine $LiBH_4$ and the (b) 25 vol.% nano ZrO_2 composite. Dashed lines show deconvolutions of the spectra with Gaussian functions. (c) ^{11}B MAS and (d) ^6Li MAS NMR spectra of pristine $LiBH_4$ and 25 vol.% nano ZrO_2 composite recorded at room temperature.

composites and pristine $LiBH_4$. The nano ZrO_2 composite showed the highest σ, 5.0×10^{-5} S·cm^{-1} at 50 °C, which was ~11,000 times higher than that of pristine $LiBH_4$ at 50 °C. The σ of the nano ZrO_2 composite was also higher than that of micron ZrO_2 composite, suggesting that an increase in the volume fraction of the interface between $LiBH_4$ and ZrO_2 significantly affects the σ. The activation energy (E_a) of ion conduction was estimated using the Arrhenius equation ($\sigma = \sigma_0 \exp(-E_a/kT)$, σ: ion conductivity, σ_0: pre-exponential factor, E_a: activation energy, k: Boltzmann constant, and T: absolute temperature). The E_a values of the nano ZrO_2 composite, micron ZrO_2 composite, and pristine $LiBH_4$ were 0.50, 0.66, and 0.85 eV, respectively. Note that the E_a values of the micron ZrO_2 composite and pristine $LiBH_4$ were derived between 30 and 115 °C. Fig. 3 shows the NMR spectra of pristine $LiBH_4$ and the nano ZrO_2 composite. Fig. 3 (a) and (b) shows ^7Li static NMR spectra at three different temperatures (−20, 24, and 50 °C). Pristine $LiBH_4$ shows a broad Gaussian peak at each temperature and the full width at half maximum (FWHM) of the peak decreased with the increase in temperature, which confirmed that Li-ion diffusion was enhanced at elevated

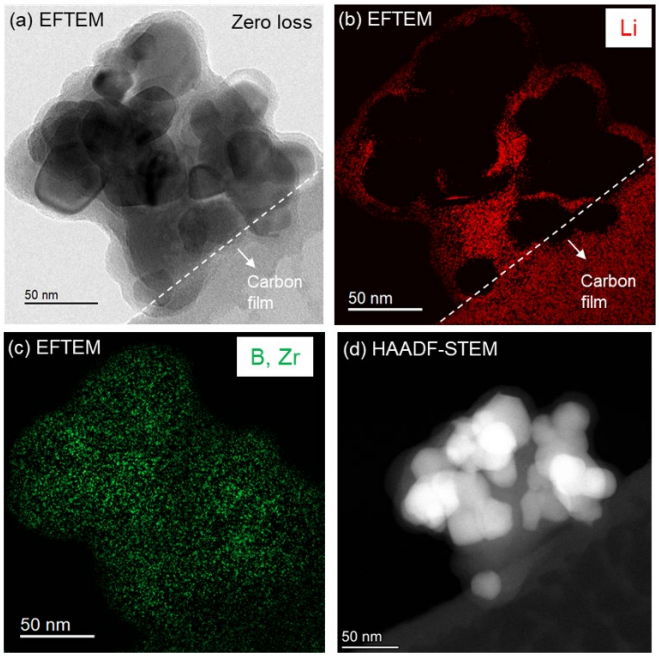

Fig. 4 (a) EFTEM zero-loss image, (b) EFTEM Li mapping, (c) EFTEM combined elemental mapping from B and Zr, and (d) HAADF-STEM image for 25 vol.% nano ZrO_2 composite. The Li K-edge was used for Li mapping, and the B K-edge and Zr $M_{4,5}$-edge were used for the combined mapping. The particles were deposited on carbon films on the TEM grids, which is indicated in the lower-right corner of the images.

temperature. The spectra in the nano ZrO_2 composite showed a two-component peak consisting of a sharp motionally narrowed peak and a broad peak. The sharp narrowed peak is associated with fast-diffusing Li ions in the structurally disordered regions along the conductor/insulator interfaces.[19] The area fractions of the narrowed component were estimated from the deconvolution of the spectra. As the temperature increased, the contribution of the sharp narrowed peak also increased. At 50 °C, ~9.2 % of the total number of Li ions participate in fast ion dynamics. To clarify the chemical bonding states, ^{11}B and ^{6}Li magic angle spinning (MAS) NMR spectra were obtained, and the results are shown in Fig. 3 (c) and (d), respectively. The peak at −41.3 ppm in the ^{11}B MAS spectra was assigned to the $[BH_4]$ species in the $LiBH_4$ phase.[14] Additionally, the spectra contain a relatively sharp small peak at 1.0 ppm and a broad less intense peak around 10 ppm. The former peak was attributed to $[B(OH)_4]$ species[20] and the latter peak originated from amorphous B-O species.[9] Unlike pristine $LiBH_4$, the amount of amorphous B-O species increased in the nano ZrO_2 composite. The formation of B-O species was also confirmed in other $LiBH_4$-oxide nanocomposites.[11,17] Moreover, a peak at −1.2 ppm was observed in the ^{6}Li MAS spectra for pristine $LiBH_4$, which corresponded to the chemical bonding states of $LiBH_4$.[14] In addition, a broad peak around −0.3 ppm was observed. This peak may be attributed to the Li-B-O species.[21] For the nano ZrO_2 composite, the peak position of $LiBH_4$ species was shifted toward positive ppm values (~−1.0 ppm), and the FWHM became broader compared with that of pristine $LiBH_4$. This downfield shift would originate from the slightly different Li environments by the existence of ZrO_2. Thus, the chemical bonding states of Li and B in the nano ZrO_2 composite were similar to those in pristine $LiBH_4$, but they were not identical.

For Li imaging in the composites, energy-filtered TEM (EFTEM) was performed. EFTEM is a form of TEM that focuses on electrons with a specific energy loss by utilizing an energy-selective slit.[22] Fig. 4 (a) shows an EFTEM zero-loss image of the as-synthesized nano ZrO_2 composite. The corresponding unfiltered TEM image is shown in Fig. S3. The particles were deposited on a carbon film on the TEM grid, and the ZrO_2 nanoparticles, which were covered with nanoscale thin films, were observed. Fig. 4 (b) shows EFTEM elemental mapping using the Li K-edge, which indicated that Li exists in the thin films. The signal from the carbon film was observed as indicated in Fig. 4 (b), which would be attributed to the noise signal from the tail of low-energy carbon plasmon peak. The Li signal was observed only for the edge of particles, but the signal on the ZrO_2 particles were not observed well, which could be due to a high-intensity background of Zr $N_{2,3}$-edge peak near Li K-edge as shown in the TEM-electron energy loss spectrum in Fig. S4. Owing to the close energies between B K-edge and Zr $M_{4,5}$-edge, the combined mapping from both B and Zr was obtained, as shown in Fig. 4 (c). The signals were observed from both ZrO_2 particles and the thin films. Fig. 4 (d) shows the high-angle annular dark-field (HAADF)-STEM image of the composite. Owing to the enhanced Z-contrast in the HAADF image, the boundary between the ZrO_2 and thin films became clearer. As shown in Fig. S5, the STEM-EDS analysis revealed that Zr exists in the ZrO_2 particles regions (Fig. S5(c)) and boron exists in the thin film regions (Fig. S5(f)). Therefore, considering the NMR and TEM results, the ZrO_2 particles were covered with nanoscale $LiBH_4$ thin films. The thickness of the $LiBH_4$ film in the nano ZrO_2 composite was less than several tens of nanometers according to the TEM observations. The $LiBH_4$ film thickness estimated by BET measurements of $LiBH_4$-metal oxide nanocomposites was between 1.4 and 46.0 nm,[12] which is consistent with the TEM results. The EFTEM and HAADF-STEM images of the nano ZrO_2 composite after ionic conductivity measurements are shown in Fig. S6. The similar particles

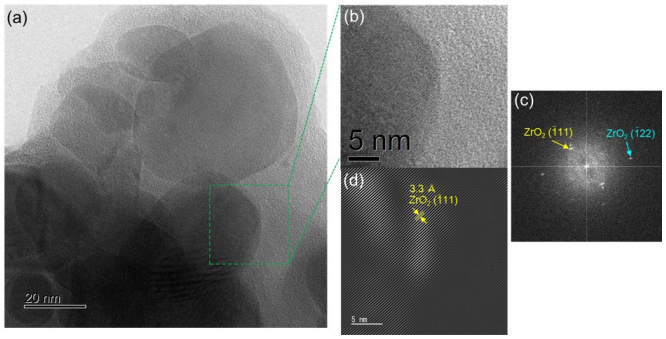

Fig. 5 (a) High-resolution TEM image of 25 vol.% nano ZrO_2 composite, (b) enlarged image of the selected area, (c) fast Fourier transform (FFT) pattern from the selected area in Fig. 5(b), and (d) Inverse FFT images from the spot indicated by a yellow arrow in Fig. 5 (c).

morphology was observed compared with the as-synthesized composite. Fig. 5 shows a high-resolution TEM image of the nano ZrO_2 composite. As shown in Fig. 5(a), the lattice fringes corresponding to crystalline ZrO_2 were observed. An enlarged image of the selected region and the corresponding fast Fourier transform analyses are shown in Fig. 5 (b-d). Lattice fringes were not observed in the thin film regions, indicating that the thin films are amorphous. This is consistent with the XRD results in Fig. 1 (a-e).

The origin of the conductivity enhancement of $LiBH_4$-oxide nanocomposites has been discussed in previous studies. Space charge layer effects are considered to be one of the reasons for the enhancement. A recent study revealed a strong correlation between the thickness of silica pore walls and the fraction of $LiBH_4$ that shows fast dynamics.[23] The effect is considered to originate from charge distributions within the silica scaffold. Another possible reason is the formation of interfacial side-reaction phases between $LiBH_4$ and oxide. This also has been proposed in a recent study,[23] where silicon-hydride-borohydride and silicon-oxide-lithium bonds are formed at the interface between $LiBH_4$ and SiO_2. The ion dynamics study of $LiBH_4$ in silica nanopores revealed the two distinct fractions.[24] One is dynamic and amorphous fraction near the silica pore walls, consists of rapidly diffusing Li^+ and $[BH_4]^-$ ions. The other is the less-dynamic and bulk-like fraction which is located in the core of the pores. From the NMR spectra in this study, both pristine $LiBH_4$ and the nano ZrO_2 composite contained Li-B-O species, but only the nano ZrO_2 composite showed fast-diffusing Li ions in the static spectra, which indicate the interface interactions between ZrO_2 and $LiBH_4$ is important. Although the Li maps were obtained by EFTEM technique, additional microscopy studies are necessary to clarify the interfacial structure. Quantification of the Li distribution and low-dose/contamination imaging may be useful for future high-resolution TEM analysis of $LiBH_4$-based materials.

In this study, the Li-ion conductivity of $LiBH_4$-ZrO_2 composite was investigated using micron ZrO_2 and nano ZrO_2 particles. The conductivity of the nano ZrO_2 composite was higher than that of the micron ZrO_2 composite. By combining $LiBH_4$ with ZrO_2, the fast-diffusing Li ions appeared in the ^{7}Li NMR spectra. However, pristine $LiBH_4$ showed a broad peak, which was typical for the slow-diffusing Li ions for the low-temperature phase of $LiBH_4$. From the MAS NMR spectra, the chemical bonding states of Li and B in the composite were similar to pristine $LiBH_4$, but a slight change was observed. This suggests that the conductivity enhancement is caused by interface interactions including space charge layer effects and/or minor interfacial side reactions. Moreover, the Li distribution in the composite was visualized on the nanoscale by energy-filtered TEM for the first time. The complementary NMR and TEM analysis confirmed that the ZrO_2 particles were covered with amorphous and nanoscale $LiBH_4$ thin films.

Part of this work was supported by “Advanced Research Infrastructure for Materials and Nanotechnology in Japan (ARIM)” of the Ministry of Education, Culture, Sports, Science and Technology (MEXT), Grant number JPMXP1223HK0022 (Hokkaido University). The authors are thankful to Mr. Naoya Nakagawa for his help in the NMR experiments and Mr. Ryo Ota for his help in the STEM observations. We thank Edanz (https://jp.edanz.com/ac) for editing a draft of this manuscript.

Conflicts of interest

There are no conflicts to declare.

Notes and references

1 R. Chen, W. Qu, X. Guo, L. Li and F. Wu, *Mater. Horiz.*, 2016, **3**, 487-516.
2 J. C. Bachman, S. Muy, A. Grimaud, H. Chang, N. Pour, S.F. Lux, O. Paschos, F. Maglia, S. Lupart, P. Lamp, L. Giordano and Y.S. Horn, *Chem. Rev.*, 2016, **116,** 140-162.
3 Y. Pang, Y. Liu, J. Yang, S. Zheng and C. Wang, *Materials Today Nano*, 2022, **18,** 100194.
4 M. Matsuo, Y. Nakamori, S. Orimo, H. Maekawa and H. Takamura, Appl. Phys. Lett., 2007, **91,** 224103.
5 D. Blanchard, A. Nale, D. Sveinbjörnsson, T.M. Eggenhuisen, M.H.W. Verkuijlen, Suwarno, T. Vegge, A.P.M. Kentgens and P.E. de Jongh, *Adv. Funct. Mater.*, 2015, **25,** 184-192.
6 W.S. Tang, A. Unemoto, W. Zhou, V. Stavila, M. Matsuo, H. Wu, S. Orimo and T.J. Udovic, *Energy Environ. Sci.*, 2015, **8,** 3637-3645.
7 S. Kim, N. Toyama, H. Oguchi, T. Sato, S. Takagi, T. Ikeshoji and S. Orimo, *Chem. Mater.*, 2018, **30,** 386-391.
8 H. Oguchi, M. Matsuo, T. Sato, H. Takamura, H. Maekawa, H. Kuwano and S. Orimo, *J. Appl. Phys.*, 2010, **107,** 096104.
9 Y. Nakagawa, T. Kimura, S. Isobe and T. Shibayama, *J. Phys. Chem. C*, 2020, **124,** 10398-10407.
10 Y.S. Choi, Y.S. Lee, K.H. Oh and Y.W. Cho, *Phys. Chem. Chem. Phys.*, 2016, **18,** 22540-22547.
11 Y.S. Choi, Y.S. Lee, D.J. Choi, K.H. Chae, K.H. Oh and Y.W. Cho, *J. Phys. Chem. C*, 2017, **121,** 26209-26215.
12 V. Gulino, L. Barberis, P. Ngene, M. Baricco and P.E. de Jongh, *ACS Appl. Energy Mater.*, 2020, **3,** 4941-4948.
13 V. Gulino, M. Brighi, F. Murgia, P. Ngene, P.E. de Jongh, R. Černý and M. Baricco, *ACS Appl. Energy Mater.*, 2021, **4,** 1228-1236.
14 R. Zettl, M. Gombotz, D. Clarkson, S.G. Greenbaum, P. Ngene, P.E. de Jongh and H.M.R. Wilkening, *ACS Appl. Mater. Interfaces*, 2020, **12,** 38570-38583.
15 R. Zettl, K. Hogrefe, B. Gadermaier, I. Hanzu, P. Ngene, P.E. de Jongh and H.M.R. Wilkening, *J. Phys. Chem. C*, 2021, **125,** 15052-15060.
16 S.M. Opalka, X. Tang, B.L, Laube and T.H. Vanderspurt, Nanotechnology, 2009, **20,** 204024.
17 Z. Liu, T. Zhang, S. Ju, Y. Ji, Z. Hu, Y. Lv, G. Xia and X. Yu, *ACS Appl. Energy Mater.*, 2022, **5,** 14301-14310.
18 J. Haruyama, K. Sodeyama, L. Han, K. Takada and Y. Tateyama, Chem. Mater., 2014, **26,** 4248-4255.
19 S. Breuer, V. Pregartner, S. Lunghammer and H.M.R. Wilkening, *J. Phys. Chem. C*, 2019, **123,** 5222-5230.
20 N. Hiraishi, M. Sayed, R. Hill, J. Tagami and F. Hayashi, *Sci. Rep.*, 2021, **11,** 15734.
21 V.K. Michaelis, K. Levin, Y. Germanov, G. Lelong and S. Kroeker, *Chem. Mater.*, 2018, **30,** 5521-5526.
22 J. Verbeeck, D.V. Dyck and G.V. Tendeloo, *Spectrochim. Acta B*, 2004, **59,** 1529-1534.
23 S.F.H. Lambregts, E.R.H. van Eck, P. Ngene and A.P.M. Kentgens, *ACS Appl. Energy Mater.*, 2022, **5,** 8057-8066.
24 S.F.H. Lambregts, E.R.H van Eck, Suwarno, P. Ngene, P.E. de Jongh and A.P.M. Kentgens, *J. Phys. Chem. C*, 2019, **123,** 25559-25569.

